Journal of Biomedical Optics

BiomedicalOptics.SPIEDigitalLibrary.org

# Voxel-based measurement sensitivity of spatially resolved near-infrared spectroscopy in layered tissues

Masatsugu Niwayama

SPIE.

Masatsugu Niwayama, "Voxel-based measurement sensitivity of spatially resolved near-infrared spectroscopy in layered tissues," *J. Biomed. Opt.* **23**(3), 030503 (2018), doi: 10.1117/1.JBO.23.3.030503.

# Voxel-based measurement sensitivity of spatially resolved near-infrared spectroscopy in layered tissues

**Masatsugu Niwayama***
Shizuoka University, Faculty of Engineering, Department of Electrical and Electronic Engineering, Hamamatsu, Japan

**Abstract.** We quantitatively investigated the measurement sensitivity of spatially resolved spectroscopy (SRS) across six tissue models: cerebral tissue, a small animal brain, the forehead of a fetus, an adult brain, forearm muscle, and thigh muscle. The optical path length in the voxel of the model was analyzed using Monte Carlo simulations. It was found that the measurement sensitivity can be represented as the product of the change in the absorption coefficient and the difference in optical path length in two states with different source–detector distances. The results clarified the sensitivity ratio between the surface layer and the deep layer at each source–detector distance for each model and identified changes in the deep measurement area when one of the detectors was close to the light source. A comparison was made with the results from continuous-wave spectroscopy. The study also identified measurement challenges that arise when the surface layer is inhomogeneous. Findings on the measurement sensitivity of SRS at each voxel and in each layer can support the correct interpretation of measured values when near-infrared oximetry or functional near-infrared spectroscopy is used to investigate different tissue structures.  [DOI: 10.1117/1.JBO.23.3.030503]

Keywords: near-infrared spectroscopy; oximetry; spatially resolved spectroscopy; voxel; sensitivity.

Paper 170729LR received Nov. 12, 2017; accepted for publication Feb. 21, 2018; published online Mar. 9, 2018.

## 1 Introduction

Tissue oximetry using near-infrared spectroscopy (NIRS) is used in a range of fields, including brain research, sports medicine, surgery, and obstetrics.[1,2] Implantable devices and devices mounted on the finger of the investigator have been developed,[3,4] and the range of tissue types that can be examined has widened. NIRS instruments apply four basic techniques: time-resolved spectroscopy (TRS), spatially resolved spectroscopy (SRS), frequency-domain spectroscopy (FDS), and continuous-wave spectroscopy (CWS). TRS, FDS, and CWS record changes in light intensity at a single point, whereas SRS is a multipoint approach. CWS, which uses an adaptation of the Beer–Lambert law, is the simplest to apply and the most widely used. Recent TRS[5] using data processing methods and high-performance FDS[6] have been developed to measure scattering and absorption coefficients, but these systems have not been widely introduced to clinical tests because it is a complex and expensive system. Both SRS and CWS are simple and low-cost approaches to light radiation and detection and benefit from a high signal-to-noise ratio. SRS is used to measure the absolute values of hemoglobin concentration, and its measurement sensitivity can be suppressed when examining superficial tissue.[7] This is because analysis is based on the difference in intensity at two points. A number of previous studies have addressed the spatial sensitivity distribution of CWS[8–11] and diffuse optical tomography (DOT).[12,13] Dehghani et al.[12] and Saikia and Kanhirodan[13] analyzed the influence of source–detector separation and depth-related sensitivity for reconstruction of DOT. However, as its voxel-based sensitivity for SRS oximetry has not yet been quantified, there is a need for further investigation of the roles played by source–detector separation and by the various layered structures of the target tissue. In the current study, we examined the SRS sensitivity in the source–detector axis direction and depth direction and compared the difference in measurement sensitivity of SRS and CWS at each voxel and layer.

## 2 Methods

On the basis of radiative transfer theory, we performed a Monte Carlo analysis of the six tissue types shown in Fig. 1. For the directly contacted cerebral tissue and the small animal brain, a source–detector separation of up to 20 mm was used. This was increased to 40 mm when tested on the fetus, adult head, and limb muscles, mimicking the separation used by commercially available instruments or reported by research studies.[1–4] Figure 1 shows the six model tissues used in the Monte Carlo analysis: (1) cerebral tissue contacted directly by an optical probe, (2) a small animal brain accessed via the scalp, (3) the forehead of a fetus, (4) an adult brain, (5) forearm muscle, and (6) thigh muscle. The optical properties shown in Table 1 and used in the simulations were based on previous literature.[14–19] To allow the simulation results to be applied to NIRS data interpretation, the models were divided into a surface part and a deep part. Figure 1(a) shows a surface to deep combination of gray matter and white matter, Figs. 1(b)–1(d) show the scalp plus gray matter and white matter, and Figs. 1(e) and 1(f) show skin and muscle. The thickness of the surface component was set to 1.5 mm to represent the scalp and skin thickness of 1 to 2 mm.[20] The sensitivity of CWS is known to be determined by the mean optical path length $L$. The relationship between path length and SRS sensitivity is as follows. $I_A$ is the light intensity detected over a short distance $\rho_A$ from the light source, and $I_B$ is the intensity detected over a longer distance $\rho_B$. As the spatial intensity slope $S$ is the difference in light intensity per unit length, $S$ is defined as $\ln(I_A/I_B)$. The change in $S$ given a change in the absorption coefficient $\mu_a$ is then defined as the measurement sensitivity of SRS. The values of $S$ are taken from optical measurements, and the unknown absorption coefficients are derived from the values of $S$ and the theoretical curves.

In Eq. (1), suffixes 1 and 2 denote values before and after the small change in absorption, respectively. The $\Delta S$ associated

*Address all correspondence to: Masatsugu Niwayama, E-mail: niwayama.masatsugu@shizuoka.ac.jp

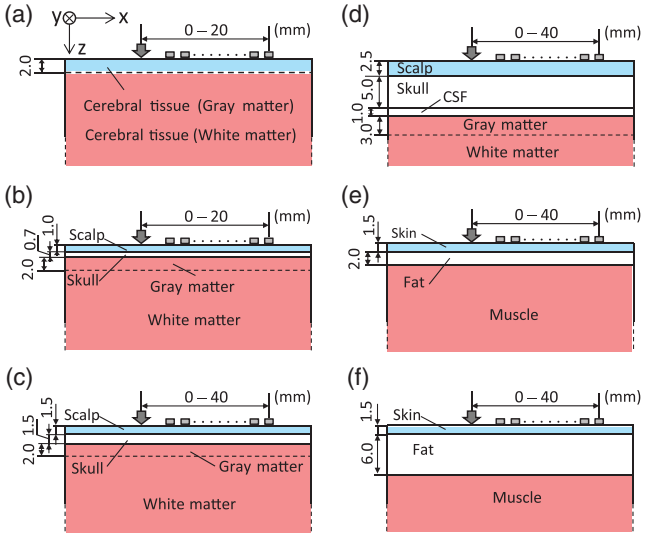


**Fig. 1** Simulation models for (a) cerebral tissue, (b) small animal brain, (c) fetal brain, (d) adult brain, (e) forearm muscle, and (f) thigh muscle.

**Table 1** Optical properties for each tissue.

| Tissue | Reduced scattering coefficient $\mu_s'$ (mm$^{-1}$) | Absorption coefficient $\mu_a$ (mm$^{-1}$) |
|---|---|---|
| Scalp | 1.3 | 0.020 |
| Skull | 2.0 | 0.010 |
| Cerebrospinal fluid | 0.3 | 0.002 |
| Gray matter | 1.6 | 0.035 |
| White matter | 5.0 | 0.015 |
| Skin | 1.3 | 0.020 |
| Fat | 1.2 | 0.003 |
| Muscle | 0.7 | 0.025 |

with a change in optical density ΔOD and the mean path lengths $L_A$ and $L_B$ is then derived as follows:

$$\begin{aligned}\Delta S &= \ln(I_{2A}/I_{2B}) - \ln(I_{1A}/I_{1B}) \\ &= \ln(I_{2A}/I_{1A}) - \ln(I_{2B}/I_{1B}) \\ &= -\Delta \mathrm{OD}_A + \Delta \mathrm{OD}_B \\ &= \Delta\mu_a(L_B - L_A). \end{aligned} \tag{1}$$

In CWS, sensitivity is usually based on the mean path length, whereas in SRS the sensitivity is also influenced by the difference between $L_A$ and $L_B$. On the basis of this relationship, the sensitivity of SRS for a small voxel at point $(x, y, z)$ is given by

$$\Delta S_{x,y,z} = \Delta\mu_a^{x,y,z}(L_B^{x,y,z} - L_A^{x,y,z}). \tag{2}$$

By preliminary analysis to investigate the slope change due to an increase in the whole $\mu_a$ or the voxel $\mu_a$ by 1%, it was verified that Eqs. (1) and (2) held when $\Delta\mu_a$ was small and the relationship between $S$ and $\mu_a$ could be regarded as linear. The sensitivity for each layer is derived by integrating the voxel values in the same layer. The SRS sensitivity for the surface and deep layers is derived as follows:

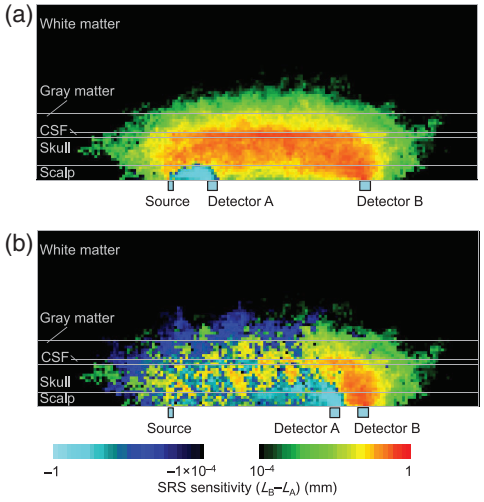


**Fig. 2** SRS sensitivity distribution from an adult head model: (a) $\rho_A = 7$ mm, $\rho_B = 35$ mm and (b) $\rho_A = 30$ mm, $\rho_B = 35$ mm.

$$\Delta S_{\mathrm{surface}} = \Delta\mu_a^{\mathrm{surface}}(L_B^{\mathrm{surface}} - L_A^{\mathrm{surface}}), \tag{3}$$

$$\Delta S_{\mathrm{deep}} = \Delta\mu_a^{\mathrm{deep}}(L_B^{\mathrm{deep}} - L_A^{\mathrm{deep}}). \tag{4}$$

For example, $L_A^{\mathrm{surface}}$ denotes the intensity-weighted average path length through the surface layer that the light detected at a position A has traversed. To clarify the influence of the change of $S$ on the oximetry, the absorption coefficient is calculated by the commonly used equation [21] as follows:

$$\mu_a \approx \frac{1}{3\mu_s'}\left(\frac{S}{\rho_B - \rho_A} - \frac{2}{\frac{\rho_A+\rho_B}{2}}\right)^2. \tag{5}$$

The concentrations of oxyhemoglobin [$O_2$Hb], deoxyhemoglobin [HHb], and tissue oxygen saturation $StO_2$ are obtained by

$$[\mathrm{O_2Hb}] = \frac{\varepsilon_{\mathrm{HHb}}^{\lambda 2}\mu_a^{\lambda 1} - \varepsilon_{\mathrm{HHb}}^{\lambda 1}\mu_a^{\lambda 2}}{\varepsilon_{\mathrm{O_2Hb}}^{\lambda 1}\varepsilon_{\mathrm{HHb}}^{\lambda 2} - \varepsilon_{\mathrm{O_2Hb}}^{\lambda 2}\varepsilon_{\mathrm{HHb}}^{\lambda 1}}, \tag{6}$$

$$[\mathrm{HHb}] = -\frac{\varepsilon_{\mathrm{O_2Hb}}^{\lambda 2}\mu_a^{\lambda 1} - \varepsilon_{\mathrm{O_2Hb}}^{\lambda 1}\mu_a^{\lambda 2}}{\varepsilon_{\mathrm{O_2Hb}}^{\lambda 1}\varepsilon_{\mathrm{HHb}}^{\lambda 2} - \varepsilon_{\mathrm{O_2Hb}}^{\lambda 2}\varepsilon_{\mathrm{HHb}}^{\lambda 1}}, \tag{7}$$

$$\mathrm{StO_2} = \frac{[\mathrm{O_2Hb}]}{[\mathrm{O_2Hb}] + [\mathrm{HHb}]}, \tag{8}$$

where $\varepsilon_{\mathrm{O_2Hb}}^{\lambda 1,\lambda 2}$ and $\varepsilon_{\mathrm{HHb}}^{\lambda 1,\lambda 2}$ are the extinction coefficients of HHb and $O_2$Hb, respectively, at the wavelengths $\lambda_1$ and $\lambda_2$.[22] In this study, the influence when the position of the absorber changes in the direction of the source–detector axis was also analyzed. We assumed two wavelengths of 770 and 830 nm and placed a $10 - \times 10 - \times 3.5$-mm hypoxic region ($StO_2$: 30%, $\mu_{a770} = 0.044$ mm$^{-1}$, $\mu_{a830} = 0.032$ mm$^{-1}$) in the normal cortex ($StO_2$: 63%, $\mu_{a770} = 0.035$ mm$^{-1}$, $\mu_{a830} = 0.035$ mm$^{-1}$).

## 3 Results and Discussion

Figure 2 shows the voxel-based sensitivity $\Delta S_{x,y,z}$ from two model detector combinations: $\rho_A = 7$ mm, $\rho_B = 35$ mm, and

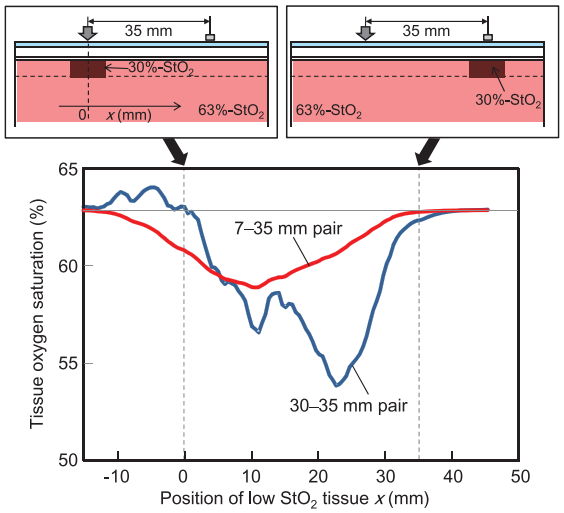


**Fig. 3** Changes in tissue oxygen saturation $StO_2$ due to position of low oxygen tissue in the source–detector axis direction.

$\rho_A = 30$ mm, $\rho_B = 35$ mm. The voxel was 0.5 mm on each side. The values of 10 voxels near the center ($-2.5 < y < 2.5$) were summed to clarify the trend. The red/yellow/green plots represent positive changes in spatial slope for a 10% increase in absorption, and the blue/cyan plots represent negative changes.

In both Figs. 2(a) and 2(b), the sensitivity of the surface layer was negative close to detector A and positive close to detector B. When blood is in the negative sensitivity area, an incorrect reverse tendency will be mixed into the calculation results of the oxygen saturation and blood volume. At a $\rho_A$ of 30 mm, a strong positive sensitivity was noted within a narrow range in the deep layer, but a small negative sensitivity appeared at the side near the light source. Figure 3 shows the oxygen saturation due to the change in the relative position between the optical probe and the 30%-StO2 region. When light was detected in a pair of 7 to 35 mm, $StO_2$ decreased by 4.5% with the approach of the low oxygen tissue. When a pair of 30 to 35 mm was used, it decreased by 8%, but $StO_2$ at $x = -5$ mm increased by 1% despite low oxygenation. These results suggest the following: (1) when the surface layer is heterogeneous, as is the case for veins, wounds, or inflammation, the effect on the measured value is large and can be positive or negative. (2) When both detectors A and B are distant from the light source, many sites have negative sensitivity, but information can be obtained from a narrow region of the deep layer. (3) When the gap between $\rho_A$ and $\rho_B$ is sufficiently long, average information can be obtained across a wide area of the deep tissue.

Figure 4 shows the measurement sensitivity of each layer from every model for both CWS and SRS. Because SRS makes use of two distances, the SRS results are plotted on the horizontal axis using $\rho_B$. The color coding corresponds to

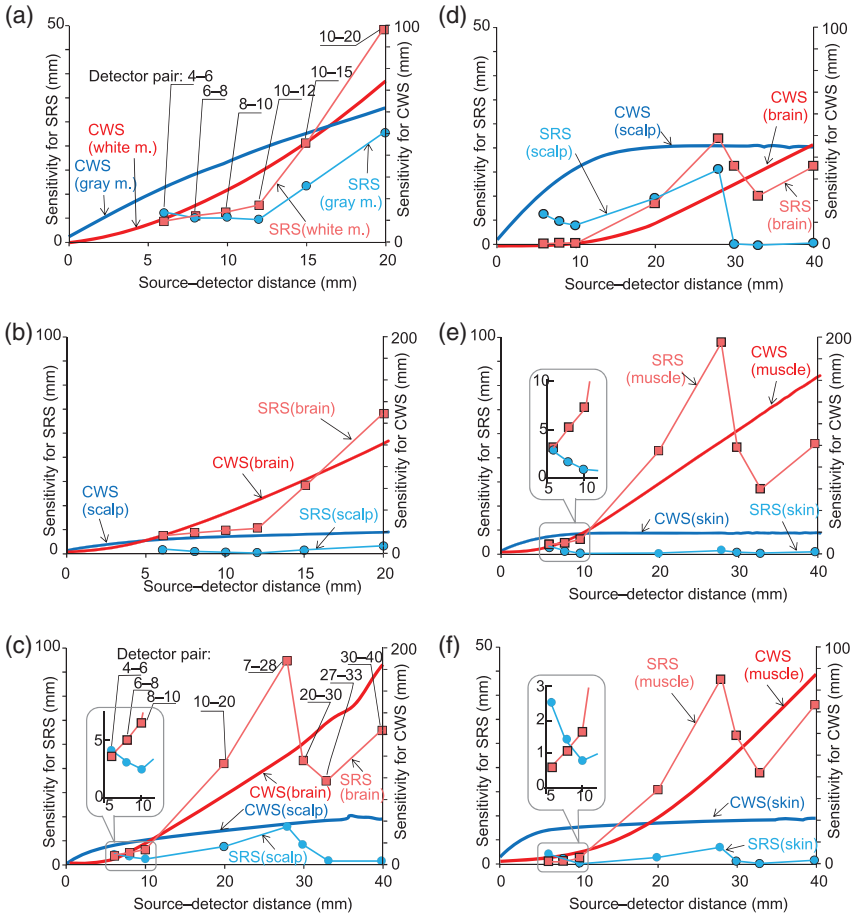


**Fig. 4** Measurement sensitivity of SRS and CWS for each model, each layer, and each detector pair. Symbols (a)–(f) correspond to Fig. 1. Detector pair of (b) is the same as (a), and pairs of (d)–(f) are shown in (c).

the color given to each layer in Fig. 1. In all the models, the CWS sensitivity for both layers and the SRS sensitivity for the deep layer increased as the source–detector distance $\rho$ increased, whereas the SRS sensitivity in the surface layer decreased. The cancelation produced by the positive and negative sensitivities reduced the sensitivity in the surface layer. In direct contact cerebral measurement [Fig. 4(a)], the region of interest is often the surface layer. When $\rho$ was <15 mm, the sensitivity of both SRS and CWS in the surface layer was greater. As shown in Figs. 4(b)–4(f), hemodynamics in the surface layer may affect the measured values. In the case of the small animal model [Fig. 4(b)], deep sensitivity was dominant, especially when using SRS. This suggests that (i) cerebral tissue can be sufficiently measured only after shaving and (ii) craniotomy is not necessary. In the fetus or neonate model brain [Fig. 4(c)], SRS measurement with the detector pair at 4 to 6 mm showed almost the same sensitivity in the surface and deep layers. Even when a probe with a $\rho$ of <10 mm was used, sensitivity in the deep layer remained relatively strong. In the model of the adult brain [Fig. 4(d)], it was necessary to set $\rho_B$ to 28 mm or more. The muscle measurement model used both thin [Fig. 4(e)] and thick [Fig. 4(f)] fat layers. The influence of skin was very slight when $\rho_B > 20$ mm. It was demonstrated that, across a wide range of conditions, the influence of the surface layer could be canceled when SRS measurement was used as long as the layer was homogeneous. To cancel the changes in the surface tissue, it is necessary to avoid applying force only near the detectors and to avoid contact with heterogeneous parts such as the subcutaneous veins. By comparing the SRS sensitivity reported in this study with the CWS sensitivity reported in earlier studies,[3,4,7–11] ways of suppressing or extracting the influence of the surface layer may be suggested.

## 4 Conclusions

The analysis results of the sensitivity of the voxel sensitivity and the influence of the low- $StO_2$ tissue position quantitatively showed one of the factors of false negative and false positive signals on NIRS that was discussed in the previous study.[23,24] By modeling actual measurements, we also compared the difference in sensitivity of each voxel and in each layer of SRS and CWS quantitatively. Measurement points and the ratio between the deep layer and the surface layer in measurement were clarified. Our findings on the measurement sensitivity of SRS at each voxel or layer can be used for hemodynamic interpretation of the measured values from different tissues.

### Disclosures

Authors have no financial interests associated with the results of this study.

### Acknowledgments

This work was supported in part by Japan Society for the Promotion of Science (JSPS) under Grants-in-Aid for Scientific Research (25350525).

### References

1. A. Villringer et al., "Near infrared spectroscopy (NIRS): a new tool to study hemodynamic changes during activation of brain function in human adults," *Neurosci. Lett.* **154**(1–2), 101–104 (1993).
2. T. Hamaoka et al., "The use of muscle near-infrared spectroscopy in sport, health and medical sciences: recent developments," *Philos. Trans. R. Soc. A: Math., Phys. Eng. Sci.* **369**(1955), 4591–4604 (2011).
3. M. Niwayama and T. Yamakawa, "Implantable thin NIRS probe design and sensitivity distribution analysis," *Electron. Lett.* **50**(5), 346–348 (2014).
4. N. Kanayama and M. Niwayama, "Examiner's finger-mounted fetal tissue oximetry," *J. Biomed. Opt.* **19**(6), 067008 (2014).
5. K. Mehta et al., "Spread spectrum time-resolved diffuse optical measurement system for enhanced sensitivity in detecting human brain activity," *J. Biomed. Opt.* **22**(4), 045005 (2017).
6. B. B. Zimmermann et al., "Frequency domain near-infrared multiwavelength imager design using high-speed, direct analog-to-digital conversion," *J. Biomed. Opt.* **21**(1), 016010 (2016).
7. L. M. L. Dix et al., "Comparing near-infrared spectroscopy devices and their sensors for monitoring regional cerebral oxygen saturation in the neonate," *Pediatr. Res.* **74**(5), 557–563 (2013).
8. E. Okada and D. T. Delpy, "Near-infrared light propagation in an adult head model. II. Effect of superficial tissue thickness on the sensitivity of the near-infrared spectroscopy signal," *Appl. Opt.* **42**(16), 2915–2922 (2003).
9. A. V. Patil et al., "Experimental investigation of NIRS spatial sensitivity," *Biomed. Opt. Express* **2**(6), 1478–1493 (2011).
10. G. E. Strangman, Z. Li, and Q. Zhang, "Depth sensitivity and source-detector separations for near infrared spectroscopy based on the Colin27 brain template," *PLoS One* **8**(8), e66319 (2013).
11. A. Messere and S. Roatta, "Influence of cutaneous and muscular circulation on spatially resolved versus standard Beer–Lambert near-infrared spectroscopy," *Physiol. Rep.* **1**, e00179 (2013).
12. H. Dehghani et al., "Depth sensitivity and image reconstruction analysis of dense imaging arrays for mapping brain function with diffuse optical tomography," *Appl. Opt.* **48**(10), D137–D143 (2009).
13. M. J. Saikia and R. Kanhirodan, "Region-of-interest diffuse optical tomography system," *Rev. Sci. Instrum.* **87**(1), 013701 (2016).
14. S. Wan, R. R. Anderson, and J. A. Parrish, "Analytical modeling for the optical properties of the skin with in vitro and in vivo applications," *Photochem. Photobiol.* **34**(4), 493–499 (1981).
15. H. R. Eggert and V. Blazek, "Optical properties of human brain tissue, meninges, and brain tumors in the spectral range of 200 to 900 nm," *Neurosurgery* **21**(4), 459–464 (1987).
16. P. Vanderzee, M. Essenpreis, and D. T. Delpy, "optical-properties of brain-tissue," *Proc. SPIE* **1888**, 454–465 (1993).
17. G. Mitic et al., "Time-gated transillumination of biological tissues and tissuelike phantoms," *Appl. Opt.* **33**(28), 6699–6710 (1994).
18. J. L. Robertson et al., "Effect of blood in the cerebrospinal fluid on the accuracy of cerebral oxygenation measured by near infrared spectroscopy," *Adv. Exp. Med. Biol.* **812**, 233–240 (2014).
19. M. Niwayama et al., "Quantitative measurement of muscle hemoglobin oxygenation using near-infrared spectroscopy with correction for the influence of a subcutaneous fat layer," *Rev. Sci. Instrum.* **71**(12), 4571–4575 (2000).
20. H. M. Hori, G. Rebora, and A. Crovato, "The thickness of human scalp: normal and bald," *J. Invest. Dermatol.* **58**(6), 396–399 (1972).
21. S. J. Matcher et al., "Absolute quantification methods in tissue near infrared spectroscopy," *Proc. SPIE* **2389**, 486–495 (1995).
22. S. J. Matcher et al., "Performance comparison of several published tissue near-infrared spectroscopy algorithms," *Anal. Biochem.* **227**(1), 54–68 (1995).
23. I. Tachtsidis and F. Scholkmann, "False positives and false negatives in functional near-infrared spectroscopy: issues, challenges, and the way forward," *Neurophotonics* **3**(3), 031405 (2016).
24. S. Greenberg, T. Shear, and G. Murphy, "Extracranial contamination of near-infrared spectroscopy devices," *Anesth. Analg.* **124**(1), 356–358 (2017).